



Peering into the structural evolution of glass-like carbons derived from phenolic resin by combining small-angle neutron scattering with an advanced evaluation method for wide-angle X-ray scattering

F. Badaczewski ^{a,1}, M.O. Loeh ^{a,1}, T. Pfaff ^a, S. Dobrotka ^b, D. Wallacher ^c, D. Clemens ^c, J. Metz ^d, B.M. Smarsly ^{a,e,*}

^a Institute of Physical Chemistry, Justus Liebig University, Heinrich-Buff-Ring 17, 35392, Giessen, Germany

^b Schunk Carbon Technology GmbH, Rodheimer Straße 59, 35452, Heuchelheim, Germany

^c Helmholtz-Zentrum Berlin für Materialien und Energie, Hahn-Meitner-Platz 1, 14109, Berlin, Germany

^d University of Applied Sciences, Campus Friedberg, Wilhelm-Leuschner-Strasse 13, 61169, Friedberg, Germany

^e Center for Materials Research (LaMa), Justus-Liebig-University, Heinrich-Buff-Ring 16, 35392, Giessen, Germany

ARTICLE INFO

Article history:

Received 8 June 2018

Received in revised form

17 August 2018

Accepted 5 September 2018

Available online 7 September 2018

ABSTRACT

The structural evolution of two non-graphitizing glass-like carbons derived from a liquid resolite and a solid novolac-type phenolic resin was quantitatively characterized by combining small-angle neutron scattering (SANS) with an advanced evaluation for wide-angle X-ray scattering (WAXS) data. Utilizing these two methods allowed for studying the microstructure on the Ångström level (graphene stacks, WAXS) and the inaccessible microporosity (SANS). The applied WAXS analysis provided quantitative structural parameters for both, size and disorder in the polyaromatic sp^2 microstructure. Hence, the combined SANS-WAXS analysis yielded comprehensive insights into the relation between the graphene microstructure and the inaccessible porosity upon heat treatment for glass-like carbons, i.e. a non-graphitizing class of carbon. In particular, the analogue investigation of a graphitizing mesophase pitch demonstrates the major impact of the chemical composition of the utilized carbon precursor. For the glass-like carbons the results revealed different growth rates for the lateral extent of the basic structural units (L_a) depending on the temperature range, finally reaching 12 nm, whereas the stack height (L_c) exhibiting 2.2 nm is hardly affected by the thermal processing up to 3000 °C. As a major finding our study thus relates the evolution of microstructure and porosity to changes in chemical composition.

© 2018 Elsevier Ltd. All rights reserved.

1. Introduction

Glass-like carbons derived from phenol-formaldehyde (PF) resins or similar thermosetting polymeric precursors represent an exceedingly import class of carbons [1]. Due to a high mechanical strength, a low density and an excellent thermal stability, glass-like carbons, and thus the initial PF resins are utilized as one of the major components for the production of carbon materials and carbon fibre reinforced carbons (CFRC), a light-weight material, that maintains a high mechanical performance even at elevated

temperatures [2]. Furthermore, glass-like carbons are typically utilized to seal open porosity, i.e. of graphite materials, to increase density and mechanical strength and to reduce permeability, as they are known to be gas-tight and exhibit an excellent chemical resistance [3].

Key physical and chemical properties of glass-like carbons, e.g. the thermal stability, the chemical resistance, the density, the Young's modulus and the thermal conductivity are directly correlated to the carbon microstructure [2,4–9]. The basic structural units (BSU) of most sp^2 -based non-graphitic carbons generally comprise finite-sized stacks of polyaromatic carbon layers, exhibiting disorder effects as depicted in Fig. 1a [10,11]. Moreover, glass-like carbons contain elevated levels of inaccessible porosity (voids) [3,12], a crucial feature for the low density as well as for energy storage applications, e.g. as active anode materials for sodium-ion

* Corresponding author. Institute of Physical Chemistry, Justus Liebig University, Heinrich-Buff-Ring 17, 35392, Giessen, Germany.

E-mail address: bernd.smarsly@phys.chemie.uni-giessen.de (B.M. Smarsly).

¹ These two authors contributed equally to this work.

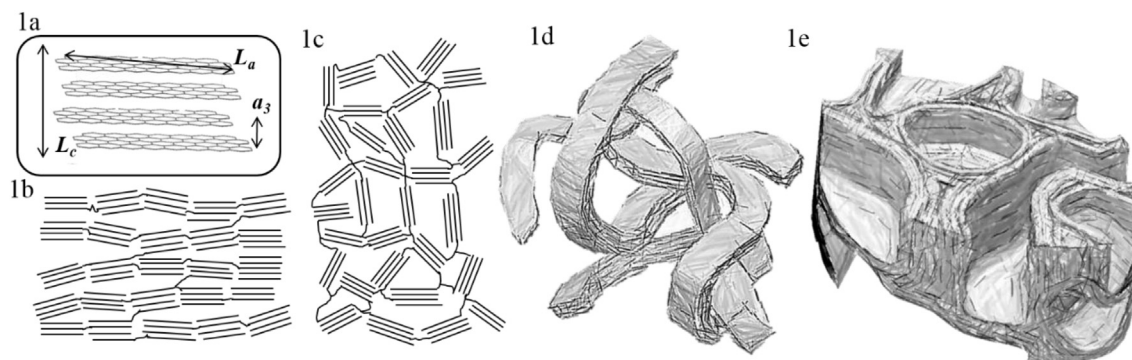


Fig. 1. a) basic structural unit (BSU) of the WAXS of a typical sp^2 carbon, composed of finite sized stacks of graphene-like layers featuring structural effects. (L_a average graphene layer size, L_c average stacking height, a_3 average interlayer spacing, 1b–c) according to the structural model proposed by R. Franklin for b) graphitizing and for c) non-graphitizing carbons [10] d) structure model for glass-like carbon consisting of ribbon like structures with frame pores as proposed by Refs. [17,18] and e) structure model for glass-like carbon comprising completely enclosed pores as proposed by Refs. [1,19].

based batteries. Here, sodium ions are supposed to penetrate the carbon skeleton and form quasi-metallic clusters in these inaccessible voids [13,14]. Consequently, besides the level of structural order, the nature of the closed porosity, i.e. the volume fraction, pore (void) size and geometry of the pores also influence the material properties. Thus, a detailed quantitative characterization of the microstructural evolution, comprising the BSU as well as porosity, is mandatory to tune process conditions which predefine the properties of the resulting carbon materials. The main process parameters impacting the microstructure are the applied heat treatment, including the temperature and residence time as well as the chemical composition of the carbon precursors [10,11,15]. As a thermosetting resin, cured PF resins are considered as non-graphitizing carbon precursors, i.e. they comprise a high degree of crosslinking, which prevents the formation of a liquid-crystalline phase during the carbonization. Thus, they maintain a non-graphitic structure even at heat treatment at temperatures of up to 3000 °C. In contrast, graphitizable carbon precursors, such as coal tar pitches or petroleum-based pitches, can be easily transformed into graphite by sufficient heat treatment [16]. Currently, different structural models are available to describe the complex bulk structure and the arrangement of the BSU for non-graphitizing glass-like carbons (Fig. 1c–e).

The first structural model for graphitizing and non-graphitizing carbon, depicted in Fig. 1a–b, was proposed by Franklin et al. [10], who suggested an approximately parallel arrangement of small and crosslinked stacks of graphene-like layers as the BSU for graphitizing carbon precursors, and a more intensely crosslinked network of randomly arranged BSUs for non-graphitizing carbons, containing voids in-between these BSU stacks. However, whereas the basic model is widely accepted for the graphitizing carbons [11,16–20], the model for the non-graphitizable carbons was further modified, as the nature of the crosslinks is not specified. At high temperatures exceeding 2500 °C, such crosslinks should be mostly removed and are insufficient to explain the inability to form graphitic lattices [1,21]. A widely accepted structure model for glass-like carbons was put forward by Jenkins et al. [17,18] in 1971 who assumed that the polymeric structure of the precursor is partially maintained in the resulting carbon. They proposed a structural model consisting of a felt-like entanglement of “narrow stacks” of curved and twisted ribbon-shaped carbon layers (Fig. 1d) [3,12]. However, the key properties of glass-like carbon, such as the impermeability to gases and the excellent chemical inertness might be difficult to explain by this model, considering the relatively high concentration of more reactive edge carbon atoms and the very open structure. Later, other groups suggested a more bulk-like model, consisting of multi-

layered curved carbon walls, which completely enclose the inaccessible voids (Fig. 1e) [1,19], to which the aforementioned properties may be more easily attributed. Newer structural models, e.g. by Harris et al. [22] additionally consider the presence of non-six-member carbon rings and propose a model consisting of discrete fragments of randomly curved Fullerene-like carbon sheets [9,23]. For glass-like carbon derived from furfuryl alcohol Jurkiewicz et al. propose a structure mainly consisting of curved sp^2 planes, enclosing voids, where the agglomeration of point defects and the presence of non-six-member rings is proposed to induce curvature [24]. The development of the degree of curvature as a function of the HTT was investigated by diffraction measurements (Wide-Angle X-ray/Neutrons) and their evaluation using atomic pair distribution functions. A more complete overview over all structure models is available in Ref. [1]. However, despite several structural models the precise microstructural evolution of glass-like carbons is still a matter of research [20].

Wide-angle X-ray scattering (WAXS) [15,16,20,21] is – next to Raman spectroscopy [9,25] and transmission electron microscopy (TEM) [11,23,26,27] – one of the few suitable techniques for the structural characterization of non-graphitic carbons, typically providing quantitative parameters such as the average interlayer spacing (a_3), the stack height (L_c) and the lateral extent of the carbon layers (L_a), which are commonly evaluated from the position and the full-width-at-half-maximum (FWHM) of the (002) and (10) reflections [21,28–30]. However, as non-graphitic carbons exhibit no crystallographic three-dimensional long-range order, WAXS patterns of these carbons usually contain no general (hkl) reflections, but only diffuse (001) and (hk) reflections in the vicinity of (hkl) reflections of graphite [31]. Furthermore, rotational and translational disorder (turbostratic disorder) within the stacking of the BSU leads to an asymmetric shape of the (hk) reflections, which often considerably overlap with the (001) reflection [32,33]. Thus, a conventional line-width based evaluation, such as the Scherrer approach is usually ambiguous and inappropriate for the evaluation of (hk) reflections. Especially for non-graphitic carbons, the line-broadening of the reflections is, besides the BSU size (L_a , L_c), also distinctly influenced by disorder effects, which are completely disregarded by conventional WAXS evaluations, i.e. Scherrer approach [27].

Therefore, the present study utilizes an advanced evaluation technique for WAXS data of non-graphitic carbons in order to attain quantitative insights into the thermally induced BSU evolution of glass-like carbons on the nanometer scale. The basic principle of this evaluation, developed by Ruland and Smarsly [31] and illustrated in Fig. 2, is based on the fitting of the whole angular range of

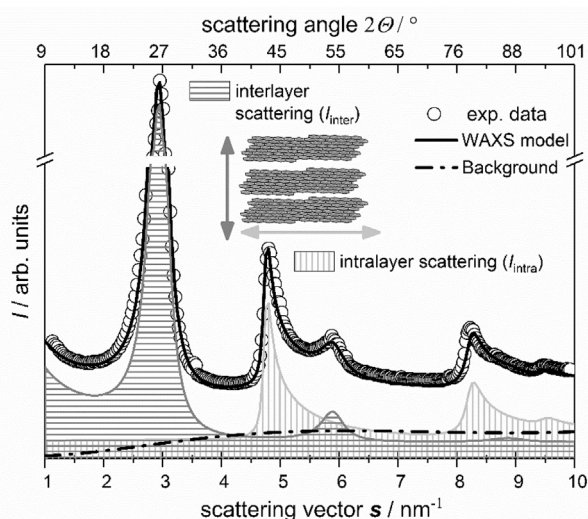


Fig. 2. Basic principle of the evaluation of the wide-angle x-ray scattering (WAXS) of non-graphitic carbon according to the Ruland and Smarsly approach; it is based on the modeling of the experimental data by a theoretical intensity distribution, consisting of a superposition of coherent intensity ($I_{\text{inter}} + I_{\text{intra}}$) and non-constant background ($I_{\text{background}}$) for a WAXS pattern of a typical non-graphitic, displaying no general (hkl) reflections, as a function of the modulus of the scattering vector $s = 2 \sin(\theta) \lambda^{-1}$.

the WAXS pattern by a theoretical WAXS function, providing a range of physically meaningful parameters describing the carbon microstructure, such as the average interlayer spacing (a_3), the average stack height (L_c), the lateral extent of the carbon layers (L_a) and the number of graphene layers per stack (N) as well as disorder effects, e.g. the average deviation of the interlayer spacing (σ_3) [34]. A complementary analysis of the micropore development upon heat treatment was conducted using small-angle neutron scattering (SANS), examining the volume fraction of the inaccessible microporosity (P), an average pore size (I_{pore}), an average wall thickness (I_{matter}) and the polydispersity of the pore shapes (κ_1) [35–37].

This study is dedicated to improving the comprehensive understanding of the entire microstructural evolution of glass-like carbons, emphasizing BSU and inaccessible microporosity, by combining results of the advanced WAXS data evaluation with SANS experiments. Here, glass-like carbons derived from two different PF resins were prepared, a self-curing liquid resole-type resin, consisting of oligomer units containing typically 2–4 monomer units as well as a solid-type resin, which consists of typically 8–12 monomer units and requires an additional curing agent. In contrast to resoles, novolac resins exhibit a phenol to formaldehyde ratio less than one. Thus, the formaldehyde, which is required for a sufficient level of crosslinking, must be provided by a curing agent, e.g. hexamethylenetetramine (HMTA), which decomposes into formaldehyde and ammonia at temperatures above approximately 85 °C. Thereby, further aspects of the present study emphasize the influence of the degree of pre-polymerization of the pristine resins as well as the influence of the presence of the curing agent on the microstructural development. Furthermore, a petroleum-based mesophase pitch is examined in order to demonstrate the influence of the chemical composition of the precursor on the microstructural evolution. In conclusion, this work aims to provide a general procedure for in-depth characterization of the microstructure of non-graphitic and non-graphitizing carbons. The pristine carbon precursors are further characterized by transmission electron microscopy (TEM), dynamic scanning calorimetry (DSC), thermogravimetric analysis coupled with mass

spectroscopy (TG-MS), elemental analysis, argon physisorption and helium pycnometry.

2. Experimental

2.1. Chemicals

Samples derived from the liquid resole and solid novolac-type PF resins are denoted as PF-R and PF-N, respectively, while the mesophase pitch sample is labeled as MP. The sample designation is completed by the corresponding heat treatment temperature (HTT), e.g. PF-R 800.

2.2. Materials

Both resins were cured in ambient atmosphere for 12 h at temperatures of 70 °C, 140 °C and 220 °C, respectively. Afterwards, the cured resins were crushed using a ball mill and the resulting powders were washed with deionized water to remove inorganic components. Subsequently, the resins and the mesophase pitch were carbonized in a nitrogen atmosphere at heat treatment temperatures (HTT) of 500 °C and 800 °C using a heating rate of 240 °C/h and a residence time of 2 h. Further heat treatment of the samples previously carbonized at 800 °C was conducted at temperatures of 1000 °C, 1200 °C, 1500 °C, 1800 °C, 2100 °C, 2300 °C and 2800 °C, utilizing a heating rate of 300 °C/h and a residence time of 2 h, too. Heat treatment at 3000 °C was carried out utilizing an Acheson furnace.

2.3. Methods

Argon physisorption measurements were conducted at 87 K using a Quantachrome Autosorb-iQ instrument coupled with a cryocooling accessory (CryoSync). The samples were pre-dried under vacuum at 250 °C for at least 4 h. Specific surface areas were determined according to the BET approach [38]. The morphology of glass-like carbon particles was examined using a Merlin scanning electron microscope from Zeiss. Thermogravimetric analysis was performed on a TG209 from Netzsch, using a heating rate of 300 °C/h. TEM images were acquired using an EM30 from Philips with an acceleration voltage of 300 kV. Elemental analysis was conducted using a Vario EL from Elementar for the determination of the carbon and hydrogen contents, whereas an Eltra model OHN2000 was used for the quantification of the oxygen content. The true density was analyzed by He-pycnometry using an AccuPyc II TEC from Micromeritics. Dynamic scanning calorimetry measurements were conducted on a DSC1-700 from Mettler-Toledo, using a heating rate of 10 °C/min and a nitrogen atmosphere. An X'Pert Pro powder diffractometer from PANalytical B.V. with Cu-K α radiation (0.15418 nm) at 40 kV and 40 mA was used for WAXS measurements in an angular range of $2\theta = 15$ –100°. For these measurements, the powder samples were flattened on a silicon single-crystal sample holder to a thickness of 1 mm. A step size of 0.1° and a scanning speed of 0.03 °s^{−1} were used for the movements.

2.3.1. Wide-angle X-ray scattering (WAXS) data evaluation

WAXS data evaluation was conducted using the approach of Ruland and Smarsly to obtain quantitative structural information from the WAXS patterns of the non-graphitic carbons. The basic concept of this approach, illustrated in Fig. 2, is only briefly summarized hereafter. A comprehensive mathematical description of underlying algorithms is beyond the scope of this work and can be found in the previous publications [31,39]. This evaluation is based on the fitting of the experimentally observed intensity (I_{obs}) over

the whole angular range through a theoretical intensity distribution normalized in electron units per carbon atom ($I_{e.u.}$):

$$I_{obs} = kAP(I_{e.u.} \otimes h_b) \quad (1)$$

where A corresponds to the absorption factor, P is the polarization factor, k is a normalization constant, h_b is a normalized distribution, which denotes instrumental broadening and \otimes represents the operation of h_b on $I_{e.u.}$. This operation can be expressed as a convolution in small ranges of the scattering angle 2θ . The theoretical intensity distribution $I_{e.u.}$ consists of contributions from coherent intensity (I_{coh}) and incoherent scattering (I_{incoh}), such as Compton scattering:

$$I_{e.u.} = I_{coh} + I_{incoh} \quad (2)$$

I_{coh} is composed of intensity contributions arising from interlayer scattering (I_{inter}), i.e. interference occurring between the different graphene-like layers in the respective stacks ($00l$ reflections) and intralayer scattering (I_{intra}), i.e. interference occurring within the 2D lattice within a graphene sheet (hk reflections):

$$I_{coh} = f_c^2 (I_{inter} + I_{intra}) \quad (3)$$

where f_c is the atomic form factor of carbon. If all carbons are organized within the graphene-like layers no further contributions of I_{coh} must be considered. The presence of non-organized atoms such as sp^3 -carbons, nitrogen or oxygen moieties, which are assumed to be statistically distributed, contribute to a non-constant background (Fig. 2) and can also be considered.

2.3.2. SANS measurements

SANS measurements were performed at the small-angle scattering instrument V16 in the cold neutron guide hall of BER-II at Helmholtz-Zentrum Berlin (HZB). The neutron flux was approximately $2 \cdot 10^6$ n/(cm² s⁻¹). All samples were measured in copper cells, exhibiting a sample volume of 0.2545 cm³ at 285 K in vacuum. A Cd-aperture of 1 cm in diameter was used, reducing the irradiated volume of the sample in the copper cells to 0.1767 cm³. The scattering data were obtained at two sample-detector distances of 1.7 m and 11.2 m, which results in a measurement range of $0.08 \text{ nm}^{-1} < s < 0.87 \text{ nm}^{-1}$, with $s = 2 \sin(\theta)/\lambda$. The software MANTID was used for the reduction of the scattering data. Thereby, the raw data were corrected for transmission as well as by subtracting the scattering of the cell background. The intensity of the raw data was further converted to absolute units (cm⁻¹) taking into account the scattering from a water standard. Further information regarding the V16 instrument can be found in Ref. [40].

2.3.3. SANS data evaluation

Assuming a single scattering process, e.g. the absence of multiple scattering, and the applicability of the kinematic scattering theory, the scattering intensity I is given by

$$I = \Im(\Delta\varrho^2) \quad (4)$$

where $\Delta\varrho$ is the difference between the local scattering neutron scattering length density at a given point in space and the average neutron scattering length density, \Im is a three-dimensional Fourier transform, 2 is the symbol for self-convolution (also termed “autocorrelation”). For a two-phase system with a constant scattering length density for both phases, the volume fractions are related to the normalized Porod invariant k by

$$k = \int_V I d\tau = 4\pi \int_0^\infty s^2 I(s) ds = V(\varrho_1 - \varrho_2)^2 \varphi_1 \varphi_2 \quad (5)$$

where $d\tau$ is the volume element in reciprocal space, s is the modulus of the scattering vector, V is the total irradiated sample volume, ϱ_i neutron scattering length density (carbon/void) and φ_i is volume fraction of phase i (carbon/void) [37]. Since the neutron scattering length of the void is zero, for porous materials the Porod invariant can be expressed as:

$$k = V(\varrho_{\text{carbon}} - \varrho_{\text{pore}})^2 \varphi_{\text{carbon}} \varphi_{\text{void}} = V\varrho_{\text{carbon}}^2 (1 - P)P \quad (6)$$

where P is the porosity. The total irradiated sample volume V was determined by

$$V = \frac{V_i \rho_{\text{appar.}}}{\rho_{\text{He}}} \quad (7)$$

where V_i is the irradiated volume of the sample cell, $\rho_{\text{appar.}}$ is the apparent density and ρ_{He} is the true density of the corresponding sample powder. General structural parameters obtainable from $I(s)$ are the average chord length (Porod length) l_p as well as the correlation length l_c [37], given by:

$$l_p = \frac{2 \int_0^\infty s^2 I(s) ds}{\pi^2 \lim_{s \rightarrow \infty} s^4 I(s)} \quad (8)$$

$$l_c = \frac{\int_0^\infty s I(s) ds}{2 \int_0^\infty s^2 I(s) ds} \quad (9)$$

Subsequently, an average pore size l_{pores} is given by the average length of segments

$$l_{\text{pores}} = \frac{l_p}{1 - P} \quad (10)$$

and the average distance between pore walls l_{matter} within the carbon material [3] can be expressed as:

$$l_{\text{matter}} = \frac{l_p}{P} \quad (11)$$

The total interface S between the domains of phases 1 and 2 is given by (see e.g. Ref. [37]):

$$\frac{S}{V} = \frac{4P(1-P)}{l_p} \quad (12)$$

and a polydispersity parameter κ_1 of the material [36] can be calculated according to Ruland by:

$$\kappa_1 = \frac{l_c}{l_p} - 1 \quad (13)$$

A well-established approach for the quantitative description two-phase systems is the so-called “chord length distributions” (CLD) $g(r)$. This method provides a statistical distribution of the distances connecting phase boundaries in pure two-phase systems, exhibiting distinct interfaces, without further assumptions regarding the pore form. Thus, the CLD is particularly suitable for the characterization of disordered porous materials. $g(r)$ is

generally related to the SANS/SAXS intensity $I(s)$ by the following relationship [47]:

$$g(r) = -8 \int_0^\infty \left(1 - \frac{2\pi^3 s^4 l_p I(s)}{k}\right) \frac{d^2}{d(2\pi rs)^2} \left(\frac{\sin(2\pi rs)}{2\pi rs}\right) ds \quad (14)$$

The Porod length l_p is the first moment of the normalized CLD, i.e.

$$l_p = \int_0^\infty r g(r) dr \quad (15)$$

Thus, l_p can be calculated by eq. (8) or (15).

The determination of $g(r)$ using eq. (14) suffers from several shortcomings, e.g. the fact that the effect of experimental noise cannot be quantified. Hence, recently an alternative approach for the calculation of $g(r)$ was developed [47], which is based on the parametrization of $g(r)$ and, thus, $I(s)$ using certain basic functions I_j and correspondingly g_j of the type

$$g(r) = \sum_{j=0}^N a_j g_j(r/b), \quad I(s) = C \sum_{j=0}^N a_j I_j(2\pi bs) \quad (16)$$

where C is a normalization constant. In essence, the experimental data $I(s)$ are fitted by I_j with the parameters a_j acting as fit parameters. This method was used in the present study to calculate CLDs and, thereof, the Porod length l_p .

The following model functions were used for the parametrization of $g(r)$ [47]:

$$g_j(r) = \frac{1}{j!} \left(\frac{r}{b}\right)^j e^{(-\frac{r}{b})}$$

For the significance of the parameter b and the details of this approach we refer to ref. [47].

3. Results and discussion

3.1. Precursors characterization

The novolac-type resin (PF-N) and the resole-type resin (PF-R) exhibit so-called solid resin contents, i.e. residual amount of solid material after curing, of 98% and 66%, respectively. Images of the pristine resins before and after curing, including the chemical structure of the curing agent, are shown in Fig. 3. The SEM images of the macroscopic particle shapes (Fig. 3) show distinct and sharp breaking edges indicating a brittle and glass-like behavior for both thermally processed resins, i.e. the glass-like carbons. Furthermore, the macroscopic geometry of the particles of the liquid resole-type resin (PF-R) are more compact and uniform compared to the particles of the solid novolac-type resin (PF-N), which suggests a different breaking mechanism during the milling. Thus, the degree of pre-polymerization and the presence of curing agent seem to influence distinctly the morphology and strength of the cured resins blocks.

Further differences between both pristine resins in the low temperature range ($< 300^\circ\text{C}$) become evident by using dynamic scanning calorimetry (DSC) to further examine the curing process, while applying a heating rate of $10^\circ\text{C}/\text{min}$ (Fig. 4). As to be expected, the glass transition temperature (T_g) of the PF-N sample noticeably exceeds that of the PF-R resin, exhibiting 24.6°C and -46.2°C , respectively. The small endothermic peak of the PF-N sample around 90°C corresponds to the beginning decomposition of HMTA or the evaporation of moisture. The progress of the curing

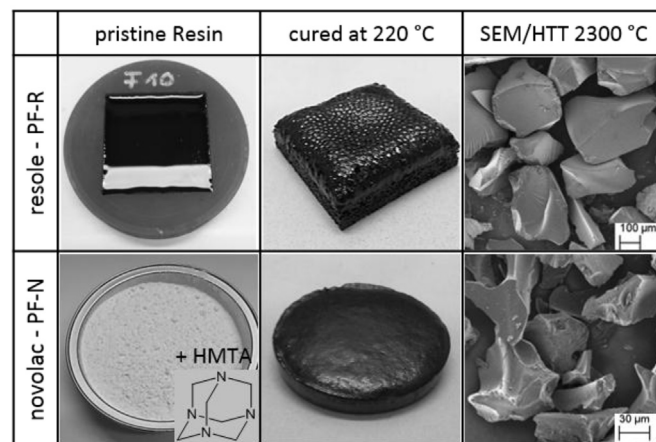


Fig. 3. Images of the resole and novolac resin before/after curing (HMTA: hexamethylenetetramine = curing agent) and SEM images of milled samples heat-treated at 2300°C .

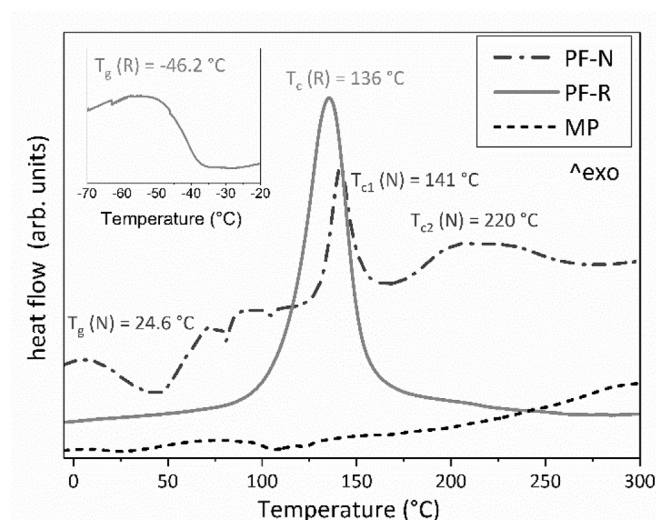


Fig. 4. DSC results of pristine phenolic resins (novolac PF-N and resole PF-R) as well as the mesophase pitch. T_g corresponds to the glass transition temperature and T_c to the reaction temperature.

reactions corresponds to the exothermic peaks, whereas the peak maximum correlates to the highest reaction rate of the curing process under the applied conditions (heating rate). Here, the investigated PF-N resin exhibits a first curing starting at temperatures above 90°C which is followed by a post-curing at temperatures between 160°C and 250°C . In contrast, the PF-R resin contains initially sufficient amounts of reactive formaldehyde, so only a single curing around 136°C occurs, which is concluded at approx. 160°C . The MP sample displays a small endothermic peak at temperatures around 105°C that can likely be attributed to the evaporation of moisture. The subsequent exothermic increase of the signal relates to the beginning decomposition of functional groups of the mesophase pitch. Therefore, basically no major reaction takes place for MP in the low temperature range, which seems reasonable considering that the production of this material typically involves temperatures exceeding 300°C .

The carbonization behavior of the cured resins and the MP in the intermediate temperature range up to 1000°C was examined by monitoring gravimetric changes (TGA, Fig. 5a). The residual

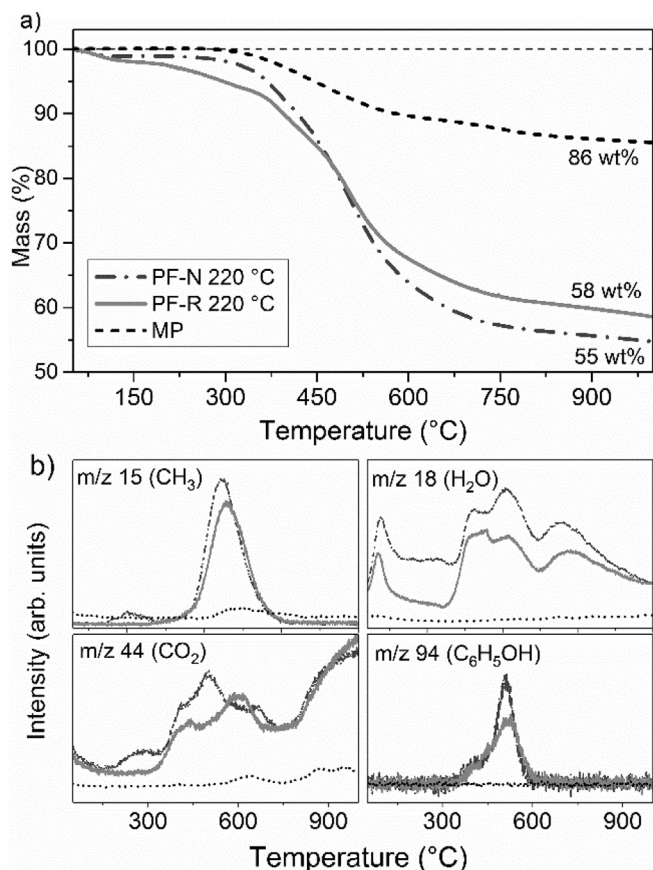


Fig. 5. a) thermogravimetric analysis b) most prominent pyrolysis gases released.

carbon amount of the precursors after the thermal decomposition processes during the carbonization corresponds to the coking yield, a crucial property for precursors utilized in the production of carbon materials. At 1000 °C, MP exhibits a coking yield of 86%, which distinctly exceeds the corresponding values of the resin precursors PF-R and PF-N, exhibiting 58% and 55%, respectively. The temperature range where pyrolysis gases are released upon thermal decomposition processes as well the amount of evolved gases are relevant parameters, as they were found to affect the microstructural evolution in the temperature range up to approximately 1200 °C [10,16,20]. Here, the corresponding main weight loss for all samples occurs in the temperature range between 350 °C and 600 °C. However, the amount of released pyrolysis gases in this range is distinctly higher for the two types of resins, which display quite similar weight loss profiles. The thermal decomposition of PF-N starts at lower temperatures than PF-R, which might be correlated to the level of crosslinking or the more complex geometry of the powder particles. The main components released during the carbonization are shown in Fig. 5b.

For these samples, the mass loss can mainly be attributed to the thermal decomposition of aliphatic groups (e.g. methylene) and of functional groups containing oxygen, causing water and carbon dioxide to be released, which continues at temperatures exceeding 1000 °C. Furthermore, in the same temperature range the emission of phenol (and derivatives, e.g. cresol) also attributes significantly to the mass loss of both PF-resins due to the breakdown of the polymer structure. These findings are in accordance with previous studies, which precisely examined the complex thermal decomposition mechanisms of similar PF-resins [41–43].

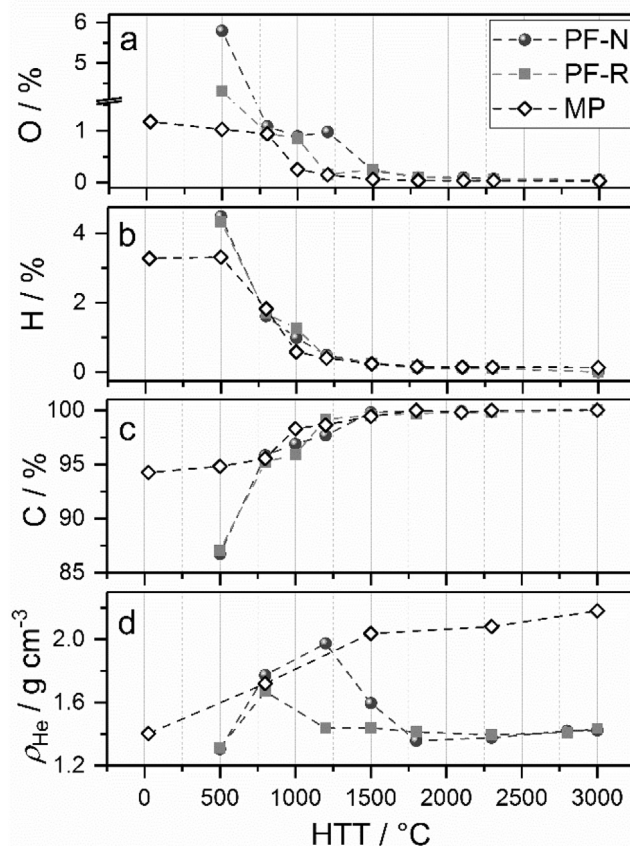


Fig. 6. Elemental analysis a) oxygen content, b) hydrogen content, c) carbon content, d) true density determined by He pycnometry (dashed lines intended only as guide-lines for the eyes). All values on elemental content are given as mass percent.

Elemental analysis was conducted to survey changes of the elemental composition up to a HTT of 3000 °C. The results are depicted in Fig. 6 and reveal distinctly higher oxygen contents for PF-N and PF-R processed at 500 °C compared to the pristine MP, exhibiting 5.8%, 4.3% and 1.2%, respectively.

For carbon materials, the oxygen content is correlated to the concentration of oxygen-containing functional groups, i.e. hydroxyl, carboxyl, epoxy and carbonyl groups, which are mostly crafted on the edges of the BSU and promote crosslinking. Substantial oxygen contents are known to strongly inhibit the structural evolution of carbon materials [26]. The TG-MS results (Fig. 5) reveal that the decomposition of such functional groups and, correspondingly, the release of carbon dioxide continues at HTT exceeding 1000 °C. The higher oxygen content of the PF-N resin is likely attributed to the phenol/formaldehyde ratio being higher than 1 during the production of the initial novolac resin, resulting in higher amounts of free phenol and hydroxyl-groups. Subsequently, an increasing HTT results in a gradually decreasing oxygen content as the decomposition of functional groups progresses (Fig. 6b). For MP, a single steep drop can be observed in the temperature range from 800 °C to 1000 °C, decreasing from approximately 1.0% to 0.1%. In contrast, both glass-like carbons display a two-step decrease in the oxygen content, the first one occurring between 500 °C and 800 °C, where all three samples show similar oxygen levels of about 1%. However, the second decrease occurs in different temperature ranges: for PR-R and PF-N the oxygen content drops to 0.2% at an HTT of 1200 °C and 1500 °C, respectively, which indicates differently bounded oxygen species or different

kinetic barriers for the release of the pyrolysis gases.

Changes of the hydrogen content are observable as well (Fig. 6b). The pristine MP sample contains 3.3%, whereas both glass-like carbons processed at 500 °C comprise roughly 4.4% hydrogen, indicating a more advanced coking process for the pristine MP sample. Subsequently, the hydrogen contents of all samples decrease to similar levels as the carbonization progresses, dropping to nearly 0.1% at 1500 °C. This drop in the hydrogen content is typically attributed to the decomposition of aliphatic side chains and other functional groups in the lower temperature range and dehydrogenation reactions of edge hydrogen atoms due to the merging of different sp^2 domains in the higher temperature range, which is correlated with the growth of the lateral BSU extent (discussed in 3.2.). The carbon content (Fig. 6c) correspondingly increases with increasing HTT and decreasing oxygen and hydrogen contents in a comparable manner for all samples.

The true density, a crucial property of glass-like carbons, which constitute a major component for light-weight CFRC materials, was investigated by helium pycnometry as a function of the HTT (Fig. 6d). A steady increase in the density of the graphitizing MP sample was observed, reaching 2.107 g cm^{-3} at 3000 °C. This increase in the true density can be utilized as a measure to estimate the graphitization degree of graphitizing carbons, which approximate the density of an ideal graphite crystal, exhibiting 2.26 g cm^{-3} , as the microstructure evolutions progresses [16]. In contrast, the non-graphitizable PF-R and PF-N display a maximum true density of 1.669 g cm^{-3} and 1.977 g cm^{-3} at 800 °C and at 1200 °C, respectively. Subsequently, the true density decreases to 1.3 g cm^{-3} at 1800 °C, which is approximately retained during subsequent thermal processing up to HTT of 3000 °C for both glass-like carbons. The true density comprises the density of the carbon skeleton, excluding all pores accessible for the helium atoms. Thus, a decrease in density with increasing HTT points to the formation of closed porosity as HTT increases, which further suggests a distinctly different course of the carbon microstructure evolution, compared to the graphitizable MP sample.

3.2. WAXS analysis of the BSU evolution

The thermally induced evolution of the BSU was mainly examined by wide-angle X-ray scattering (WAXS). The corresponding WAXS patterns at different HTT are shown in Fig. 7 as a function of the modulus of the scattering vector (s) which is directly related to the scattering angle 2θ by $s = 2 \sin(\theta) \lambda^{-1}$. WAXS patterns of the samples processed at 2800 °C are shown in Figure S1 (supporting information). Even at a HTT of 3000 °C, the WAXS patterns of both PF-derived glass-like carbons display no general (hkl) reflections, but only diffuse and mostly overlapping (001) and (hk) reflections, which is a typical feature of non-graphitizable and non-graphitic carbons. Gradually increasing the HTT results in more pronounced reflections and less overlapping, which indicates growing of the BSU as well as decreasing disorder. Here, the MP sample displays distinguishably more pronounced (001) reflections at distinctly lower HTT compared to the WAXS patterns of the glass-like carbon, qualitatively suggesting a more progressive growth of the stack height (L_c) for the MP sample. Furthermore, at a HTT of 3000 °C the MP sample becomes graphite, comprising crystallographic long range 3D order and hence displaying all reflections expected for a hexagonal graphitic lattice according to the IUPAC definition [44]. However, a precise grasp of microstructural features is challenging for these disordered materials, as the WAXS patterns at each respective HTT are similar, displaying asymmetric and strongly overlapping (hk) and (001) reflections. Therefore, an advanced evaluation approach was utilized to extract quantitative information out of these WAXS patterns. The evaluation is based on

the fitting of the entire angular range of the WAXS measurement [31]. The corresponding fits (Fig. 7) are in reasonable agreement with the experimental data.

However, as this approach is exclusively designed for non-graphitic carbons, MP samples processed at HTT exceeding 2100 °C were not evaluated by this method due to their increasingly graphitic structure [45]. The results of the advanced WAXS evaluation are displayed (Fig. 8) for the most important parameters usually utilized to describe the BSU of carbon materials as well as the main disorder contributions, which are the average stack height (L_c), the average lateral extent (L_a), the average interlayer spacing (a_3), the standard deviation of the interlayer spacing (σ_3) and the standard deviation of the next-neighbor distribution (σ_1). Further parameters are summarized in Tables S1–S3 (supporting information). The results reveal a distinctly different BSU evolution for the graphitizing MP sample compared to both PF-derived glass-like carbons, which display an approximately identical structural growth, indicating an almost negligible influence of the initial composition on the BSU development, i.e. degree of pre-polymerization as well as of differences in the curing process (Fig. 3).

The results for the average lateral extent of the BSU (L_a) are shown in Fig. 8a. We observed a moderate increase of L_a in the lower temperature range, increasing from 1 nm at a HTT of 500 °C to approximately 3.0 nm at 1000 °C for all three samples. For the graphitizing MP sample this trend is followed by a very slow growth of L_a up to a HTT of 1200 °C, after which a rapid increase of L_a , raising from 3.1 nm at 1200 °C to 12.5 nm at 2100 °C, can be observed. In contrast, the non-graphitizing glass-like carbons exhibit a very slow growth of L_a up to a higher HTT of 1500 °C, which is followed by another moderate growth phase, increasing from approx. 3 nm at 1500 °C to 6.0 nm at 2300 °C. Beyond this HTT the glass-like carbons also show a rapid increase in L_a , reaching ca. 12 nm at 3000 °C.

According to the previous work by Emmerich et al. [21] the slow and moderate growth of L_a at lower temperatures can mainly be attributed to the natural growth of existing sp^2 -layers by incorporation of carbon atoms, which are not yet organized in the sp^2 -structure, i.e. crosslinking groups or functional groups. However, this contribution becomes gradually less important as the HTT increases and the amount of not yet organized carbon atoms decreases, which is confirmed by our WAXS analysis. If the concentration of crosslinking groups between BSU is sufficiently low, the merging of different BSU is assumed to be responsible for the rapid growth of L_a . As a consequence, the rapid L_a growth of the MP sample at comparatively low HTT above 1200 °C and the second moderate L_a growth of glass-like carbons at HTT above 1500 °C might be related to the decrease in the oxygen content (Fig. 5). Furthermore, disorder and defects were not be accounted for in the work of Emmerich et al. [21], but should be considered, because they affect the lateral growth of the BSU. Here, the standard deviation of the next-neighbor distribution (σ_1) allows for an estimate of the level of disorder within the graphene-like layers (Fig. 8d). The parameter σ_1 decreases with increasing HTT, which indicates an increasing level of order within the layers. Consequently, the gradual reduction of defects and stress within the layers increases the extent of the coherent sp^2 -domains visible for diffraction-based analysis and thereby contributes to the growth of L_a . Therefore, σ_1 drops rapidly from approximately 0.017 nm at 500 °C to nearly 0.012 nm at 1000 °C, which is followed by a slow decrease of σ_1 up to 1500 °C. Beyond this HTT, σ_1 continues to decrease steadily for the MP sample, reaching 0.006 nm at 2100 °C, whereas the decrease of σ_1 seems to be limited for both glass-like carbons, reaching only 0.009 nm at 3000 °C. Thus, the results indicate that non-graphitizing glass-like carbons exhibit an intrinsically more limited potential for the removing of disorder compared to the

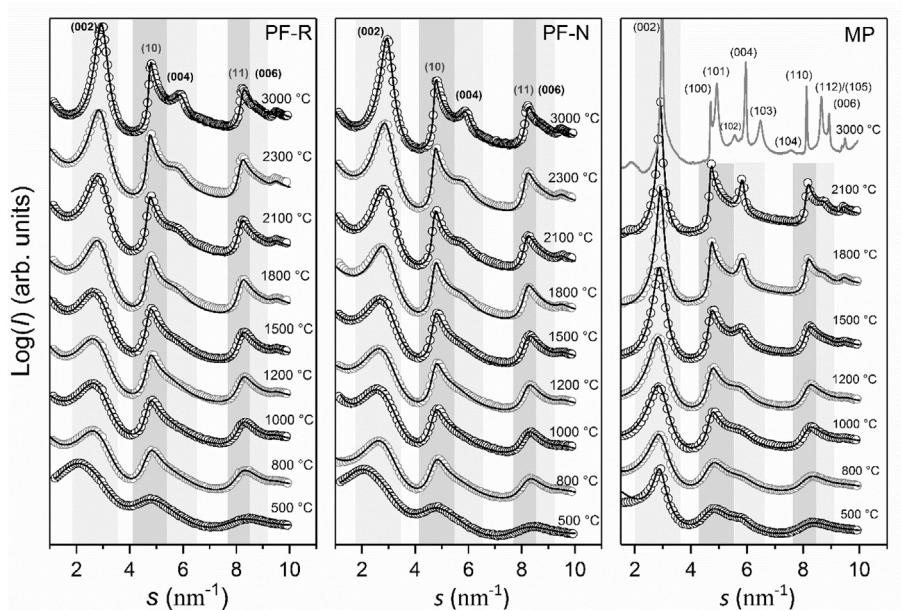


Fig. 7. WAXS data (open circles), fitting curves (lines) a) resolite-based glass-like carbon (PF-R), b) novolac-based glass-like carbon (PF-N) and c) mesophase pitch-based carbon (MP, *MP3000 experimental data (line) and the reference card for graphite JCPD 01-75-1621).

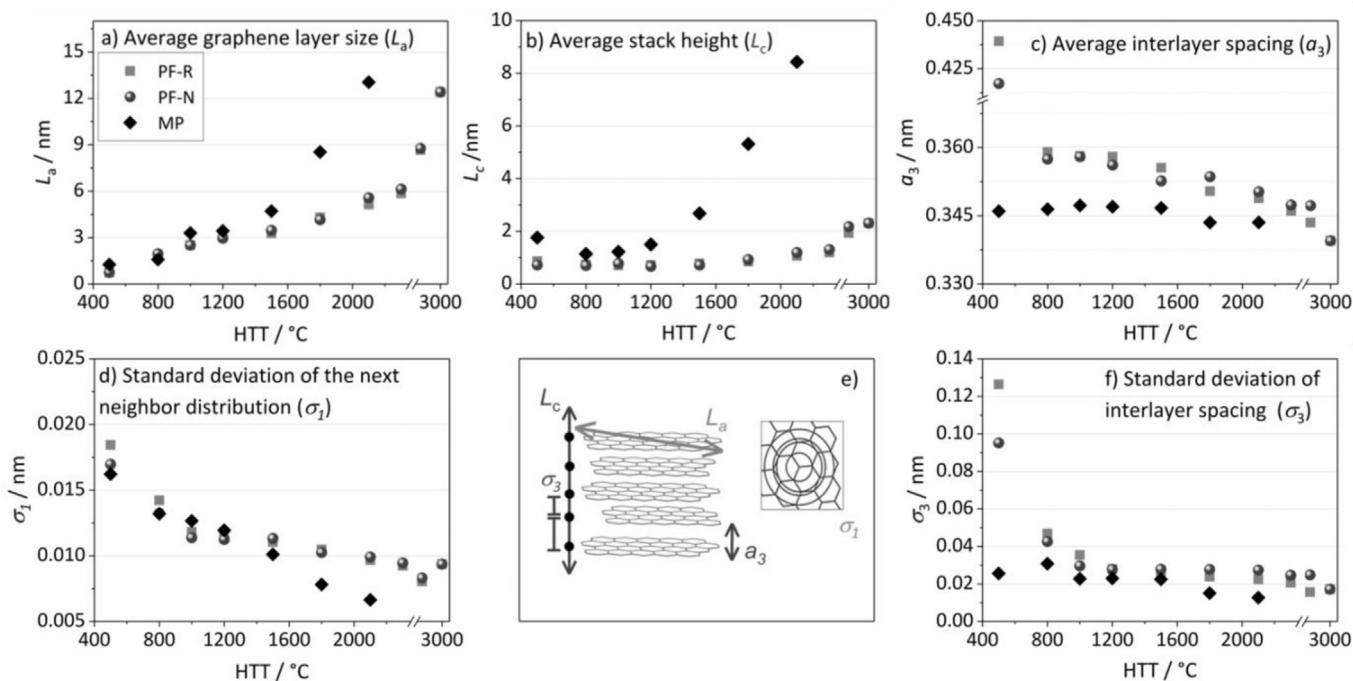


Fig. 8. WAXS modeling results, a) average layer size L_a (± 10 –15%), b) average stack height L_c (± 10 –15%) and c) average interlayer spacing a_3 (± 1 –2%), d) standard deviation of the next-neighbor distribution σ_1 (± 10 –15%), e) illustration of the parameters, f) standard deviation of the interlayer spacing σ_3 (± 10 –15%) as a function of the heat treatment temperature (HTT). The error was estimated by observing the entire fit curve, while gradually changing one of the parameters. The main aspect for the assessment of the accuracy of the fit was the divergence of a homogenous statistical deviation of experimental data and the fit curve over the whole angular range [39].

graphitizing MP. Furthermore, the results reveal a relation between the decrease in σ_1 and an increase in L_a in the respective temperature ranges, further indicating the importance of disorder for the lateral BSU growth.

In contrast to L_a , the average stacking height (L_c) of the glass-like carbons, displayed in Fig. 8b, is hardly affected by the thermal processing, growing from 0.7 nm at 500 °C to 1.4 nm at 2300 °C.

This result indicates that no significant movement and reorganization of BSU layers seems to occur over a broad range of HTT. The high degree of crosslinking within the cured resins inhibits such growth in the resulting glass-like carbons during carbonization and prevents the formation of a liquid-crystalline phase, being necessary for large-scale rearrangement of different layers [26,46]. A noticeable growth of L_c to 2.2 nm can only be observed at further

increasing HTT to 3000 °C. These results are in good agreement with the qualitative interpretation of the WAXS data, the glass-like carbons only displaying weak (001) reflections over a broad range of HTT (Fig. 7). MP shows a very different behavior, exhibiting $L_c = 1.8$ nm at 500 °C, which subsequently drops to 1.1 nm at 800 °C before L_c rapidly increases to 8.4 nm at 2100 °C and 14.4 nm* at 3000 °C (*based on the Scherrer analysis on the (004) reflection). The temporary decrease of L_c can likely be attributed to the coalescence of highly ordered mesophase domains, exhibiting a pronounced stacking, which are disturbed by the release of pyrolysis gases during the final phase of the coking process [11,16].

Another key parameter typically utilized to evaluate the progress of the BSU development is the average interlayer spacing (a_3), which gradually approaches the interlayer spacing of ideal graphite (0.335 nm) as the microstructural evolution advances [30]. At 500 °C the interlayer spacing of PF-N and PF-R, exhibiting 0.417 nm and 0.439 nm, respectively, distinctly exceeds the interlayer spacing of MP of 0.346 nm. After a large drop to about 0.359 nm at 800 °C for both glass-like carbons, a_3 remains at this level up to a HTT of 1200 °C, after which a_3 slowly decreases with increasing HTT, reaching 0.344 nm at 2300 °C. Here, the first drop of a_3 is likely correlated with the decomposition of the aliphatic and oxygen containing groups, which are grafted on the edges of BSU or act as crosslinks between BSU and thereby prevent the convergence of the layers at lower HTT. After removing these sterically demanding groups, a more ordered stacking becomes possible. Noticeably, at 3000 °C a_3 drops to roughly 0.340 nm for both glass-like carbons. In contrast, for MP a_3 remains at approximately 0.344 nm up to HTT of 2100 °C, indicating a more ordered stacking than in the mesophase domains (Fig. 8b). Additionally, the relatively low amount of pyrolysis gases released during the early stages of the thermal processing (Fig. 4) suggests lower contents of sterically demanding groups, but may still disturb a significant decrease in a_3 . At an HTT of 3000 °C, MP displays a graphitic structure and correspondingly exhibits an interlayer spacing of 0.336 nm (evaluated from the position of the (004) reflection) being close to that of an ideal graphite crystal.

The disorder present within the stacking of the BSU can be estimated by the parameter σ_3 , which describes the standard deviation of the distribution of the interlayer spacing (Fig. 8f). At 500 °C, σ_3 for the PF-N and PF-R samples distinctly exceeds σ_3 of the MP sample, exhibiting 0.096 nm, 0.126 nm and 0.026 nm, respectively, suggesting a more disordered and less homogeneous stacking in case of the glass-like carbons. The decomposition of crosslinking groups during subsequent thermal processing first leads to a significant drop of σ_3 down to 0.028 nm at 1200 °C for glass-like carbons, which then gradually decreases to 0.017 nm at 3000 °C. Consequently, although almost no growth of the stacking height L_c can be observed, the degree of order in the BSU can be enhanced by increasing the HTT. For the MP sample a slight increase in σ_3 can be observed at 800 °C, which is accompanied by the reduction of L_c in the same temperature range due to the coalescence of mesophase domains. Thereafter, σ_3 gradually decreases to 0.013 nm at 2100 °C as the HTT increases. Over a temperature range from 500 °C to 2100 °C, MP displays a generally lower level of stacking disorder, which seems reasonable considering the previous results. Thus, comparable to the disorder within the layers σ_1 , the glass-like carbons seem to possess a limited potential for removing stacking disorder.

Overall, the results revealed that a noticeably faster progress of the BSU evolution for MP occurs mainly at higher temperatures. Furthermore, the degree of pre-polymerization of the initial PF resin precursors as well as the presence of a curing agent hardly influence the BSU development of the resulting glass-like carbons. Therefore, applying the approach of Ruland and Smarsly to evaluate

the WAXS patterns of glass-like carbons and the MP allows a precise quantitative description of the structural progress of the BSU over a very broad temperature range. Thereby, contributions of disorder effects on the FWHM of WAXS reflections as well as the asymmetry of the overlapping (hk) reflections are considered instead of classical line-width based evaluation methods. Thus, this work shows that this evaluation approach provides a powerful tool to compare the microstructure of non-graphitic carbons, exhibiting very similar scattering patterns.

3.3. SANS analysis of the void evolution

Besides BSU dimension and level of atomic order, porosity also greatly contributes to the overall microstructure and thus significantly impacts crucial properties of the glass-like carbons, such as the density and the mechanical performance. Therefore, the thermally induced changes of the porosity, including voids within the carbon structure, were investigated by SANS. The results are summarized in Table 1 and the obtained scattering curves are depicted in Fig. 9a and b as a function of the modulus of the scattering vector s . Here, the scattering signal at high s is gradually reduced with increasing HTT, which directly indicates the disappearance of smaller structures, i.e. micropores. For glass-like carbons, a major part of the porosity is expected to be inaccessible porosity [4,9], especially at higher HTT (>1200 °C). Therefore, Ar-physisorption measurements were performed to examine the presence of accessible microporosity, which contributes to the externally specific surface area (Table 1). The results reveal that BET surface areas rapidly drop to less than 1 m²/g for HTT exceeding 800 °C. Consequently, the contribution of externally accessible micropores is negligible at higher HTT and the majority of pores analyzed by SANS consist of voids within carbon matter, as indicated by Helium density measurements.

The chord length distribution ($g(r)$, CLD), applicable for materials comprising two homogenous phases, i.e. void/carbon, was determined by fitting the SANS data with model functions I_j according to equation (16), the precise procedure of which is described in Ref. [47].

For PF-N (Fig. 9c) $g(r)$ exhibits a large value $g(0)$, which indicates a high degree of angularity of the material-pore interface. This angularity is gradually reduced with increasing HTT as the $g(0)$ contributions decreases, suggesting increasingly smooth pores. For PF-N heat-treated at 800 °C, $g(r)$ decreases rapidly to approx. zero at $r = 2.5$ nm, which further points to the presence of considerable amounts of smaller structures as well as the absence of structures larger than at $r = 2.5$ nm (Fig. 9d). Subsequently, $g(r)$ increases at larger r with increasing HTT and thereby the point where $g(r)$ becomes zero shifts to approximately 5 nm at 3000 °C. In general, $g(r)$ itself is not a pore-size distribution, but contains contributions from both, pores and matter. However, for small porosities, the CLD is indeed dominated by the pores, thus providing the length-scale of the voids. Our analysis thus indicates the formation of larger structures along with the reduction of smaller structures as the thermal treatment progresses, i.e. the increase of the voids.

At this point it should be noted that the calculation of the CLD is only possible and meaningful for “two-phase systems”, i.e. materials with two phases of different average densities. Hence, the CLD calculation requires the presence of the Porod asymptote ($1/s^4$) at large s , which however can be superimposed by other contributions for larger scattering angles in the small-angle scattering region, and which must be considered for the determination of porosity parameters and the CLD analysis. As outlined by Ruland [3], 1-D density fluctuations of the interlayer spacing (a_3) result in an additive scattering contribution being proportional to $1/s^2$ [3,47,48], which superimposes the Porod law and which needs to be

Table 1
Results of the SANS data evaluation. P (porosity), l_p (Porod length), l_c (correlation length), l_{pores} (pore size), l_{matter} (pore wall thickness), L_c (av. stack height - WAXS), S/V (specific surface area), κ_1 (polydispersity of pore geometry) as well as BET surface areas from argon physisorption measurements (S_{BET}), the true density (ρ_{He}) and apparent density ($\rho_{apparent}$) results. *determined by eq. (8), +determined as the first moment of $g(r)$, i.e. eq. (15).

Precursor	PF-N						PF-R		MP
HTT	800	1500	1800	2100	2850	3000	2100	2850	2100
P	0.05	0.05	0.05	0.06	0.07	0.08	0.07	0.08	0.01
l_p^*/nm	0.5	0.5	0.6	0.8	1.4	1.5	0.9	1.3	1.2
l_p from $g(r)^+/nm$	0.6	0.6	0.7	0.8	1.4	1.4	0.9	1.4	1.1
l_c/nm	0.7	0.9	1.0	1.2	2.1	2.5	1.2	2.1	5.0
l_{pores}/nm	0.6	0.6	0.6	0.9	1.5	1.4	0.9	1.4	1.3
l_{matter}/nm	1.0	1.1	1.1	1.3	2.0	1.7	1.3	1.6	7.6
$L_c, waxes/nm$	0.7	0.7	0.9	1.2	2.3	2.3	1.1	2.0	8.4
$S/V/m^2\text{ cm}^{-3}$	362	360	330	339	204	213	290	226	52
κ_1	0.4	0.6	0.6	0.5	0.6	0.8	0.4	0.6	3.0
$S_{BET}, Ar\text{-}Phys/m^2\text{ g}^{-1}$	2	<1	<1	<1	<1	<1	<1	<1	5
$\rho_{He}/g\text{ cm}^{-3}$	1.773	1.594	1.357	1.376	1.419	1.423	1.402	1.435	2.081
$\rho_{app}/g\text{ cm}^{-3}$	0.49	0.49	0.49	0.49	0.49	0.49	0.79	0.86	0.58

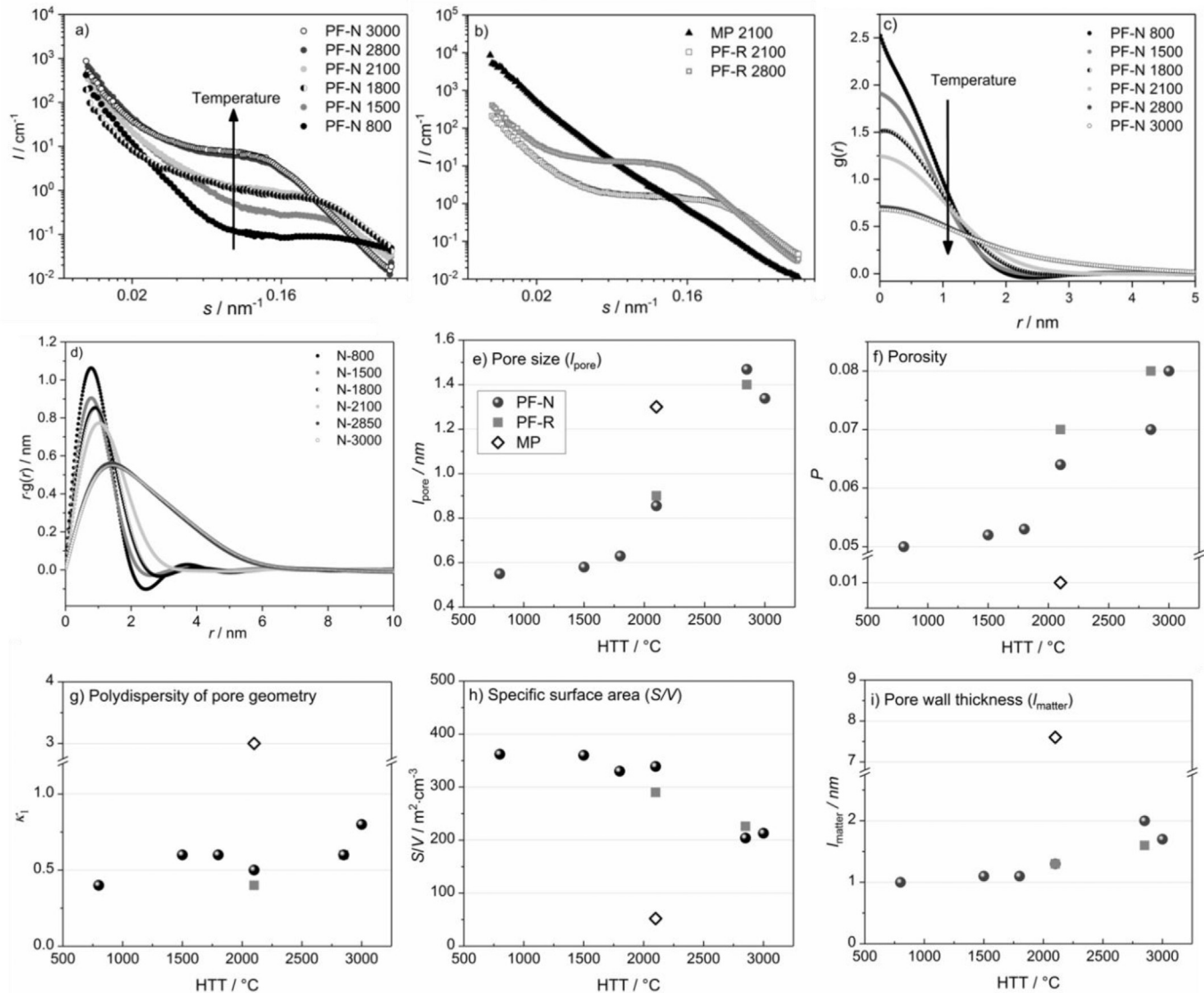


Fig. 9. a-b) SANS scattering curves, c) chord length distributions d) $r \cdot g(r)$ -plot, e) pore size (l_{pore}) f) porosity (P), g) polydispersity of the pore geometry (κ_1), h) specific surface area (S/V), i) pore wall thickness (l_{matter}) as a function of the heat treatment temperature (HTT).

thoroughly taken care of in any quantitative analysis of small-angle scattering data. The influence of this contribution on the SANS data as well as the corresponding CLD-fit are shown representatively for PF-R 2100 in Figure S2 (supporting information). For low heat treatment temperatures, the $1/s^2$ contribution is quite significant, but these fluctuations as well as their impact on the SANS analysis decrease, as revealed by the advanced WAXS analysis providing the parameter σ_3 , which quantifies the disorder in the graphene stacking. In particular, an $s^2 \cdot I$ -plot (Figure S3) shows that an $1/s^2$ contribution alone cannot account for the behavior of the SANS data at large s . It is found (Fig. 8f and Table S1 and S2) that σ_3 markedly decreases with increasing HTT, and also the $1/s^2$ contribution in the SANS data becomes less significant. The chord length distributions of PF-R, heat-treated at 2100 °C and 2800 °C, as well as of MP 2100 °C are displayed in Figure S4 (supporting information).

The results of the SANS analysis for the characterization of the micropore development are summarized in Fig. 9e–i. The average pore size (l_{pore} , Fig. 9e), increases with increasing HTT by nearly a factor of 2.5, reaching 1.4 nm at 3000 °C for PF-N. This growth of the pore size is likely attributable to a thermodynamically driven minimization of surface energy which results in the disappearance of smaller pores for the benefit of larger ones. The PF-R sample displays a similar growth of l_{pore} , exhibiting 1.4 nm at 2800 °C. The values of l_{pore} for PF-N at the lower temperatures are quite small, being in the region of 0.6 nm up to 1800 °C. Taking into account that the average interlayer spacing amounts to ca. 0.35 nm, an average pore size of 0.6 nm seems to be implausible, but is consistent with earlier studies and also the slit-like shape of the voids. Taking into account the reasonable data quality and the experimentally accessible range s , the uncertainty in the parameters l_p , k , and l_c is of the order of 10% at maximum, as obtained from the procedure described in ref. [47]. Since the other parameters are derived from these parameters (see equation (5)–(13)), the other parameters possess an uncertainty of ca. 10% as well.

Noticeably, the overall porosity, i.e. the void concentration (P , Fig. 9f), determined from the absolute intensity of the scattering signal according to equation (6), gradually increases similar to the pore size (l_{pore}) with increasing HTT. Likewise, the normalized Porod invariant (k), calculated from equation (6), also increases with HTT, which additionally indicates an increase in porosity (Figure S5, supporting information). This raise of porosity may be explainable, considering that the thermally induced internal shrinkage of the material is influenced by the geometric distribution of the carbon walls as the orientation of the walls is assumed to be statistically homogenous [1,18,19]. Inside the carbon walls (BSU) shrinkage mainly occurs in axial direction (L_c) and is limited in the lateral direction (L_a). Thus, the contribution of internal shrinkage of the carbon phase apparently exceeds the macroscopic shrinkage, leading to growing voids (l_{pores}), resulting in an increase in porosity. Although MP exhibits a distinctly lower overall porosity, l_{pore} is similar to the glass-like carbons (1.3 nm at 2100 °C). For graphitizable carbon precursors this likely originates from large slit-like pores located between the parallel arranged BSU [47,49].

Furthermore, the shape of the voids is hardly affected up to HTT of 2100 °C, which can be seen by parameter κ_1 , describing the polydispersity of the pore geometry (Fig. 9g). At even higher HTT a slight increase in κ_1 can be observed, indicating a less uniform void shape. The decreasing homogeneity of the pore shapes (κ_1) as well as the increase in the mean pore size (l_{pores}) is also in excellent agreement with the $r \cdot g(r)$ plot of the CLD analysis, where the presence of increasingly larger structures can be observed at higher HTT (Fig. 9d). Still, the angularity of the voids and carbon phase becomes increasingly smooth ($g(0)$ in Fig. 9c) despite the less homogenous void shapes. The specific surface area (S/V), displayed in

Fig. 9h, decreases with increasing HTT, dropping from 362 m²/cm³ at 800 °C to 213 m²/cm³ at 3000 °C for PF-N, which seems reasonable, considering the increasing pore size (Fig. 9e) and the decreasing angularity of the material-pore interface (Fig. 9c). Due to the lower overall porosity (P), MP exhibits distinctly smaller specific surface areas of about 50 m²/cm³. The pore wall thickness (l_{matter}), calculated from equation (9), is only moderately affected by the HTT, increasing from 1.0 nm at 500 °C to 1.7 nm at 3000 °C (Fig. 9i). These l_{matter} values are in good agreement with WAXS results for the BSU stack height (L_c) and suggest that carbon walls separating two voids mostly consist of one single BSU. Hence, BSU are orientated parallel towards the pores, i.e. the lateral BSU extent (L_a) directly surrounds the void, which is in good agreement with previous results [3,12]. Thus, the reduction of the interlayer spacing (a_3) as well as the increasingly ordered stacking (σ_3) should mainly contribute to the macroscopic shrinkage of the material. Additionally, the contribution of the gradually decreasing a_3 to the enlargement of the voids is even higher compared to the macroscopic shrinkage. The graphitizing MP sample processed at 2100 °C exhibits a distinctly higher wall thickness of 7.6 nm, which is also in good agreement with WAXS analysis.

In summary, SANS analysis provided detailed information on the thermally induced changes of the void structure, i.e. the inaccessible porosity. The results are in good accordance with several characteristic properties of glass-like carbons, illustrating the impermeability to gases, the excellent chemical and thermal resistance as well as low densities. Thus, optimal properties and correspondingly the most suitable process conditions can be identified only by combining analysis of the carbon microstructure (BSU) as well as of the inaccessible porosity therein. For instance, for sodium ion storage applications the best compromise between suitably large interlayer spacings, necessary for the intercalation of sodium ions, and void concentration for high storage capacity can be estimated [14].

3.4. TEM analysis

Representative lattice fringe images of the investigated PF-N and MP samples respectively heat-treated at 3000 °C and 2100 °C (Fig. 10) directly illustrate the differences between the carbon microstructures of a non-graphitizable precursor processed at 3000 °C and a graphitizable precursor processed at 2100 °C. Even at

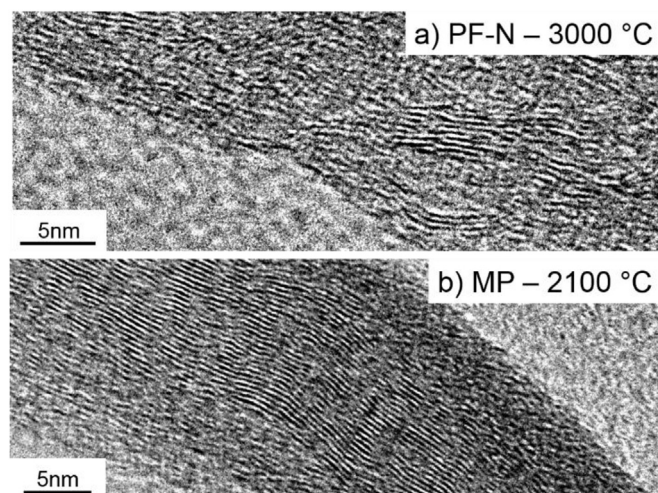


Fig. 10. TEM images a) novolac-based glass-like carbon at a HTT of 3000 °C, b) mesophase pitch based carbon at a HTT of 2100 °C.

distinctly lower HTT, the graphitizable MP sample displays comparatively large and ordered BSU, but no evident porosity. However, larger slit-like pores may still be present. In contrast, the lattice fringe of the glass-like carbon displays noticeably smaller BSU domains which frame larger voids. The dimensions shown in the TEM images are in a reasonably good agreement with the quantitative results obtained by WAXS and SANS analysis.

4. Conclusions

The evolution of the entire carbon microstructure of glass-like carbons, including the growth of the basic structural units of the carbon phase, finite sized stacks of graphene like layers exhibiting disorder effects, as well as the development of inaccessible porosity within the carbon phase were quantitatively characterized as a function of the heat treatment temperature by, for the first time, combining an advanced method of WAXS data evaluation with SANS analysis. Two types of non-graphitizing glass-like carbons, derived from an initially liquid resole-type and an initially solid novolac-type phenolic resins as well as a graphitizing mesophase pitch were investigated. The main results for the structural evolution are illustrated in Fig. 11 and can be summarized as follows:

1. For glass-like carbons, derived from a novolac- and a resole-type phenol formaldehyde resin, WAXS analysis revealed an almost identical evolution of the carbon microstructure (BSU) after 800 °C, which is hardly affected by the degree of pre-polymerization and the presence of the curing agent of the not yet cured resins.
2. Depending on the temperature range, different growth rates for the lateral BSU extent (L_a) could be observed comprising several growth contributions, namely from incorporation of free carbon atoms, the merging of different BSU and the healing of strain

and defects (σ_1). These effects all result in increasingly ordered and enlarged coherent sp^2 -domains (L_a) visible for WAXS analysis.

3. In contrast, the number of layers per stack and, correspondingly, the average stack height (L_c) remains almost constant over a broad temperature range (up to HTT of 2300 °C), indicating that the movement or reorganization of layers is strongly inhibited for the non-graphitizing glass-like carbons. Consequently, the structure initially present within the cured resin precursors seems to be nearly maintained throughout the subsequent thermal processing, which is in good agreement with previous assumptions (Fig. 1d) [18].
4. However, the interlayer spacing (a_3) gradually decreases and becomes more homogenous (σ_3). Although nearly no change of the stack heights occurs, the degree of disorder within the stacking can be reduced during the thermal processing.
5. SANS results revealed a gradually increasing pore size (l_{pore}) as well as a growing inaccessible porosity with increasing HTT, which was attributed to the thermodynamically driven disappearance of smaller pores for the benefit of larger ones, along with an inhibited macroscopic shrinking of the material due to the geometrically homogeneous arrangement of the pore walls containing BSU.
6. Voids become more smooth and larger, the latter resulting in a larger polydispersity of pore geometry, which is indicated less homogeneous in their as the angularity of the pore-carbon interface decreases ($g(0)$) and the polydispersity of pore geometry (κ_1) increases. Correspondingly, the inner specific surface area (S/V) declines with increasing HTT.
7. The pore wall thickness (l_{matter}) seems to be closely related to L_c and indicates that two voids are separated only by one single BSU, where the lateral BSU extend (L_a) directly faces the pore.

Consequently, in the authors opinion, these findings, especially the orientation of BSU and pores, best match with the concept of a bulk-like material, dominated by mostly planar multi-layered carbon walls, which completely enclose the inaccessible porosity (comparable to Fig. 1e) [1,19]. However, it must be noted that the applied WAXS analysis based on the approach of Ruland and Smarsly [31] assumes planar sp^2 -domains (BSU) and does not allow taking into account curvature of the graphenes. Thus, the presence of potentially curved sp^2 -structures comprising the presence of non-six membered rings cannot be considered here, but are assumed to be part of the microstructure of glass-like carbons, i.e. in the form of curved sp^2 -crosslinks connecting coherent domains [9]. Yet, we believe that the glass-like carbons investigated in the present study do mainly consist of planar graphene stacks and that curved stacks represent a much smaller fraction. These results are confirmed by our TEM investigations (Fig. 10), revealing a mostly planar arrangement of the graphenes and a comparably small curvature. This interpretation is in excellent agreement with TEM studies of Kübel et al., who directly observed large amounts of the aforementioned planar coherent domains in phenolic resin derived glass-like carbon [23].

To conclude, in this study a comprehensive understanding of thermally induced microstructural changes in glass-like carbon derived phenolic resin could be obtained, which leads to a better understanding of this complex material and the influence of the heat treatment temperature as a synthesis parameter. Moreover, this study confirms and partially expands previous works [3,21], as the advanced WAXS analysis provides a precise analysis of the lateral BSU extent (L_a) despite the asymmetric shape and the considerable overlapping of the (hk) reflections. Additionally, this analysis considers disorder contributions. Thereby, the obtainable information noticeably exceeds what can be obtained from classical

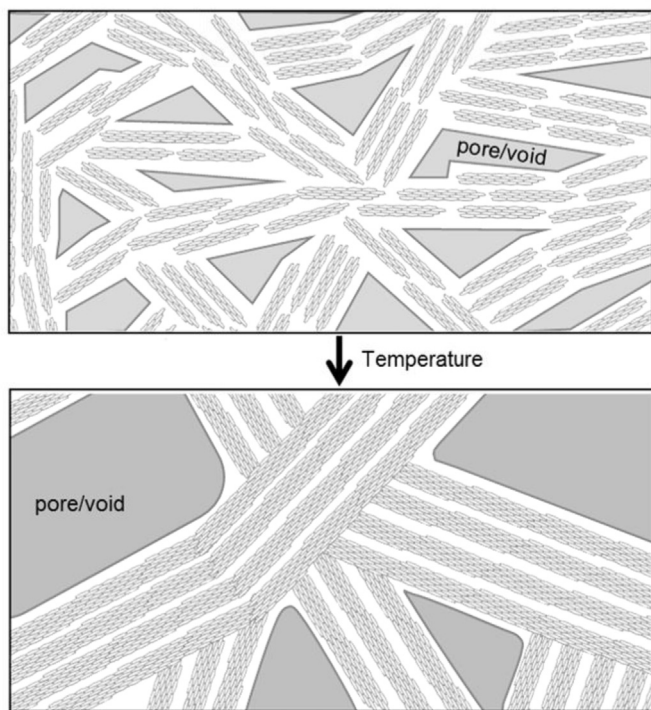


Fig. 11. Summary of the WAXS and SANS results for the microstructural evolution of a non-graphitizing PF-based glass-like carbon, emphasizing the development of carbon phase (BSU) and the inaccessible pore structure as a function of heat-treatment temperature, without depicting the presence of crosslinking groups.

line-width based analysis. However, it should be noted that not all parameters could be determined with reasonable precision for the investigated carbons. Nevertheless, the parameters directly describing the actual BSU lattice (for the graphene lattice L_a , σ_1 and for the layer stacking L_c , d_3 , σ_3) were determined with adequate accuracy. Thereby, the quantitative results of these parameters are in good agreement with the qualitative interpretation of the wide-angle X-ray scattering curves as well as the SANS and TEM characterization, further demonstrating the accuracy of the Ruland and Smarsly approach. This approach provides an easily available method for the structural characterization of disordered carbon and is especially advantageous for the comparison of different non-graphitizing and non-graphitic carbons and is now available as a software tool [50].

Acknowledgements

We thank Schunk Carbon Technology for providing the resin samples. Financial support is provided by the German Research Foundation (DFG) via the GRK (Research Training Group) 2204 “Substitute Materials for sustainable Energy Technologies”. We would like to acknowledge the Center for Materials Research (LaMa) at Justus Liebig University Giessen for the support of this project. The authors thank HZB for the allocation of neutron radiation beamtime and thankfully acknowledge the financial support from HZB.

Appendix A. Supplementary data

Supplementary data related to this article can be found at <https://doi.org/10.1016/j.carbon.2018.09.025>.

References

- [1] P.J.F. Harris, Structure of non-graphitising carbons, *Int. Mater. Rev.* 42 (1997) 206–218.
- [2] S.-S. Tzeng, Y.-G. Chr, Evolution of microstructure and properties of phenolic resin-based carbon/carbon composites during pyrolysis, *Mater. Chem. Phys.* 73 (2002) 162–169.
- [3] R. Perret, W. Ruland, X-ray small-angle scattering of glassy carbon, *J. Appl. Crystallogr.* 5 (1972) 183–187.
- [4] E. Fitzer, W. Schaefer, The effect of crosslinking on the formation of glasslike carbon from thermosetting resins, *Carbon* 8 (1970) 353–364.
- [5] R. Kumar, S.R. Dhakate, R.B. Mathur, The role of ferrocene on the enhancement of the mechanical and electrochemical properties of coal tar pitch-based carbon foams, *J. Mater. Sci.* 48 (2013) 7071–7080.
- [6] M. Inagaki, M. Toyoda, T. Tsumura, Control of crystalline structure of porous carbons, *RSC Adv.* 4 (2014) 41411–41424.
- [7] M. Inagaki, H. Orikasa, T. Morishita, Morphology and pore control in carbon materials via templating, *RSC Adv.* 1 (2011) 1620–1640.
- [8] M. Inagaki, M. Toyoda, Y. Soneda, S. Tsujimura, T. Morishita, Templated mesoporous carbons: synthesis and applications, *Carbon* 107 (2016) 448–473.
- [9] K. Jurkiewicz, M. Pawlyta, D. Zygadło, D. Chrobak, S. Duber, R. Wrzaliak, et al., Evolution of glassy carbon under heat treatment: correlation structure–mechanical properties, *J. Mater. Sci.* 53 (2018) 3509–3523.
- [10] R.E. Franklin, Crystallite growth in graphitizing and non-graphitizing carbons, *Proc. Roy. Soc. Lond.* 209 (1951) 196–218.
- [11] A. Oberlin, Carbonization and graphitization, *Carbon* 22 (1984) 521–541.
- [12] Bose S, Bragg RH. Kinetics of pore coarsening in glassy carbons. *Carbon* 1981;19:289–295.
- [13] M. Dahbi, N. Yabuuchi, K. Kubota, K. Tokiwa, S. Komba, Negative electrodes for Na-ion batteries, *Phys. Chem. Chem. Phys.* 16 (2014) 15007–15028.
- [14] S. Komaba, W. Murata, T. Ishikawa, N. Yabuuchi, T. Ozeki, T. Nakayama, et al., Electrochemical Na insertion and solid electrolyte interphase for hard-carbon electrodes and application to Na-ion batteries, *Adv. Funct. Mater.* 21 (2011) 3859–3867.
- [15] M.O. Loeh, F. Badaczewski, M. von der Lehr, R. Ellinghaus, S. Dobrotka, J. Metz, et al., Hard-templating of carbon using porous SiO₂ monoliths revisited – quantitative impact of spatial confinement on the microstructure evolution, *Carbon* 129 (2018) 552–563.
- [16] G.M. Jenkins, K. Kawamura, Structure of glassy carbon, *Nature* 231 (1971) 175–176.
- [17] G.M.K.K. Jenkins, L.L. Ban, Formation and structure of polymeric carbons, *Proc R Soc London Ser A* 327 (1972) 501–507.
- [18] A. Yoshida, Y. Kaburagi, Y. Hishiyama, Microtexture and magnetoresistance of glass-like carbons, *Carbon* 29 (1991) 1107–1111.
- [19] M.O. Loeh, F. Badaczewski, K. Faber, S. Hintner, M.F. Bertino, P. Mueller, et al., Analysis of thermally induced changes in the structure of coal tar pitches by an advanced evaluation method of X-ray scattering data, *Carbon* 109 (2016) 823–835.
- [20] P. Ouzilleau, A.E. Gheribi, P. Chartrand, The graphitization temperature threshold analyzed through a second-order structural transformation, *Carbon* 109 (2016) 896–908.
- [21] F.G. Emmerich, Evolution with heat treatment of crystallinity in carbons, *Carbon* 33 (1995) 1709–1715.
- [22] P.J.F. Harris, S.C. Tsang, High-resolution electron microscopy studies of non-graphitizing carbons, *Philos. Mag. A* 76 (1997) 667–677.
- [23] S. Sharma, C.N.S. Kumar, C. Kübel, Evolution of Glassy Carbon Microstructure : in situ transmission electron microscopy of the pyrolysis process, *Condens Matter - Mater Sci* (2018) arXiv preprint arXiv:1801.01785, <https://arxiv.org/abs/1801.01785?context=cond-mat.mtrl-sci>.
- [24] K. Jurkiewicz, S. Duber, H.E. Fischer, A. Burian, Modelling of glass-like carbon structure and its experimental verification by neutron and X-ray diffraction, *J. Appl. Crystallogr.* 50 (2017) 36–48.
- [25] G.A. Zickler, B. Smarsly, N. Gierlinger, H. Peterlik, O. Paris, A reconsideration of the relationship between the crystallite size L_a of carbons determined by X-ray diffraction and Raman spectroscopy, *Carbon* 44 (2006) 3239–3246.
- [26] A. Oberlin, S. Bonnamy, P. Rouxhet, Colloidal and supramolecular aspects of carbon, in: P.L. Walker Jr., L.R. Radovic (Eds.), *Chemistry and Physics of Carbon*, vol. 26, Dekker, New York, 1999, pp. 1–148.
- [27] A. Sharma, T. Kyotani, A. Tomita, Comparison of structural parameters of PF carbon from XRD and HRTEM techniques, *Carbon* 38 (2000) 1977–1984.
- [28] H. Honda, K. Kobayashi, S. Sugawara, X-ray characteristics of non-graphitizing-type carbon, *Carbon* 6 (1968) 517–523.
- [29] K. Kobayashi, S. Sugawara, M. Toyoda, H. Honda, An X-ray diffraction study of phenol-formaldehyde resin carbons, *Carbon* 6 (1968) 359–363.
- [30] N. Iwashita, M. Inagaki, Relations between structural parameters by x-ray powder diffraction of various carbon materials, *Carbon* 31 (1993) 1107–1113.
- [31] W. Ruland, B. Smarsly, X-ray scattering of non-graphitic carbon : an improved method of evaluation, *J. Appl. Crystallogr.* 35 (2002) 624–633.
- [32] B.E. Warren, X-ray diffraction in random layer lattices, *Phys. Rev.* 59 (1941) 693–698.
- [33] J. Biscoe, B.E. Warren, An X-ray study of carbon black, *J. Appl. Phys.* 13 (1942).
- [34] K. Faber, F. Badaczewski, M. Oschatz, G. Mondin, W. Nickel, S. Kaskel, et al., In-depth investigation of the carbon microstructure of silicon carbide-derived carbons by wide-angle X-ray scattering, *J. Phys. Chem. C* 118 (2014) 15705–15715.
- [35] S. Mascotto, D. Kuzmich, D. Wallacher, M. Siebenbürger, D. Clemens, S. Risse, et al., Poly(ionic liquid)-derived nanoporous carbon analyzed by combination of gas physisorption and small-angle neutron scattering, *Carbon* 82 (2015) 425–435.
- [36] W. Ruland, Small-angle X-ray scattering of two-phase systems: significance of polydispersity, *J. Appl. Crystallogr.* 43 (2010) 998–1004.
- [37] R. Perret, W. Ruland, X-ray small-angle scattering of non-graphitizable carbons, *J. Appl. Crystallogr.* 1 (1968) 308–313.
- [38] M. Thommes, Physical adsorption characterization of nanoporous materials, *Chem. Ing. Tech.* 82 (2010) 1059–1073.
- [39] K. Faber, F. Badaczewski, W. Ruland, B.M. Smarsly, Investigation of the microstructure of disordered, non-graphitic carbons by an advanced analysis method for wide-angle X-ray scattering, *ZAAS* 640 (2014) 3107–3117.
- [40] K. Vogtt, M. Siebenbürger, D. Clemens, C. Rabe, P. Lindner, M. Russina, et al., A new time-of-flight small-angle scattering instrument at the Helmholtz-Zentrum Berlin: V16/VSANS, *J. Appl. Crystallogr.* 47 (2014) 237–244.
- [41] H. Jiang, J. Wang, S. Wu, Z. Yuan, Z. Hu, R. Wu, et al., The pyrolysis mechanism of phenol formaldehyde resin, *Polym. Degrad. Stabil.* 97 (2012) 1527–1533.
- [42] J. Wang, H. Jiang, N. Jiang, Study on the pyrolysis of phenol-formaldehyde (PF) resin and modified PF resin, *Thermochim. Acta* 496 (2009) 136–142.
- [43] K. Trick, T.E. Saliba, S.S. Sandhu, A kinetic model of the pyrolysis of phenolic resin in a carbon/phenolic composite, *Carbon* 35 (1997) 393–401.
- [44] J. Maire, J. Mering, Graphitization of soft carbons, in: P.L. Walker Jr. (Ed.), *Chemistry and Physics of Carbon*, vol. 6, Dekker, New York, 1970, pp. 125–189.
- [45] P. Adelhelm, K. Cabrera, B.M. Smarsly, On the use of mesophase pitch for the preparation of hierarchical porous carbon monoliths by nanocasting, *Sci. Technol. Adv. Mater.* 13 (2012), 015010.
- [46] H. Marsh, C.S. Latham, The chemistry of mesophase formation, *Pet. Carbons* (1986) 1–28.
- [47] B. Smarsly, M. Antonietti, T. Wolff, Evaluation of the small-angle x-ray scattering of carbons using parametrization methods, *J. Chem. Phys.* 116 (2002) 2618–2627.
- [48] E. Hoinkis, E.B.F. Lima, P. Schubert-Bischoff, A study of carbon black corax N330 with small-angle scattering of neutrons and X-rays, *Langmuir* 20 (2004) 8823–8830.
- [49] A.F. Thunemann, Microvoids in Polyacrylonitrile Fibers: a Small-angle X-ray Scattering Study, 2000, pp. 1848–1852.
- [50] T. Pfaff, M. Simmermacher, B.M. Smarsly, CarbX: a program for the evaluation of wide-angle X-ray scattering data of non-graphitic carbons: A, *J. Appl. Crystallogr.* 51 (2018) 219–229.